

Simultaneous Denoising and Registration for Accurate Cardiac Diffusion Tensor Reconstruction from MRI

Valeriy Vishnevskiy¹, Christian Stoeck²,
Gábor Székely¹, Christine Tanner¹, and Sebastian Kozerke²

¹ Computer Vision Laboratory, ETH Zurich, Switzerland
{valeryv,tanner,szekely}@vision.ee.ethz.ch

² Institute for Biomedical Engineering, University and ETH Zurich, Switzerland
{stoeck,kozerke}@biomed.ee.ethz.ch

Abstract. Cardiac diffusion tensor MR imaging (DT-MRI) allows to analyze 3D fiber organization of the myocardium which may enhance the understanding of, for example, cardiac remodeling in conditions such as ventricular hypertrophy. Diffusion-weighted MRI (DW-MRI) denoising methods rely on accurate spatial alignment of all acquired DW images. However, due to cardiac and respiratory motion, cardiac DT-MRI suffers from low signal-to-noise ratio (SNR) and large spatial transformations, which result in unusable DT reconstructions. The method proposed in this paper is based on a novel registration-guided denoising algorithm, that explicitly avoids intensity averaging in misaligned regions of the images by imposing a sparsity-inducing norm between corresponding image edges. We compared our method with consecutive registration and denoising of DW images on a high quality *ex vivo* canine dataset. The results show that the proposed method improves DT field reconstruction quality, which yields more accurate measures of fiber helix angle distribution and fractional anisotropy coefficients.

Keywords: denoising, registration, sparsity, primal-dual, DW-MRI.

1 Introduction

Scanning time and subject motion is considered one of the most challenging issues in DW-MRI of the brain [1]. In cardiac *in vivo* DW-MRI breathing and cardiac motion requires shorter acquisition windows which lowers image SNR relative to applications in the brain [2]. Most of DT-MRI denoising algorithms are based on a model of the acquisition process, assuming spatial alignment of the individual DW images. However, image registration is challenging for low SNR. Moreover out-of-plane motion can occur during the acquisition process.

Most of the joint image denoising and registration methods apply explicit or implicit image intensity averaging [3,4,5]. Yet direct averaging can degrade denoising results and is not applicable for DW-MRI data. A novel graph-based approach was proposed by Lombaert and Cheriet in [6], where registration and

denoising are combined (via Cartesian product) for a joint label space. The advantage of this method over independent denoising and registration has been shown. Yet its applicability is questionable due to the size of the resulting label space (e.g. 256 “denoising” labels \times 1681 displacements $\in \{-20, -19, \dots, 20\} = 4308736$ labels). Logcut framework [7] might be able to efficiently solve the problem in such a huge label space, but it needs nontrivial tuning for each problem class, which has not been performed to date. Moreover, many image registration regularization measures cannot be expressed with binary energy potentials.

In our simultaneous registration and denoising method we impose the similarity of image gradients instead of intensities using sparsity inducing ℓ_1 -norm and linear representation of the image warping operator. Our main motivation is following: (a) gradients are less sensitive to intensity variations and (b) “sparse” constraints automatically “allow” images to be different in some regions, which helps us to correctly treat misalignments and heterogeneities of the images.

2 Methods

2.1 Denoising

The relation of intensity of DW image \mathbf{y}_i at spatial location s with diffusion gradient \mathbf{g}_i and diffusion tensor \mathbf{D}_s is given by the following equation:

$$\mathbf{y}_i[s] = \mathbf{y}_0[s] \exp(-b \mathbf{g}_i^\top \mathbf{D}_s \mathbf{g}_i), \quad (1)$$

where \mathbf{y}_0 is the image without diffusion weighting and b is the b -value. Given a sequence of DW images degraded with noise, the set of aligned DW images $\hat{\mathbf{y}}_i$ for N different gradient directions \mathbf{g}_i , is obtained using the following MAP estimation formulation [8]:

$$\underset{\mathbf{y}_1, \dots, \mathbf{y}_N}{\text{minimize}} - \sum_{i=1}^N \log p(\hat{\mathbf{y}}_i | \mathbf{y}_i) + \lambda \text{TV}_\phi(\mathbf{y}_1, \dots, \mathbf{y}_N), \quad (2)$$

here $p(\hat{\mathbf{y}}_i | \mathbf{y}_i)$ is a likelihood function that captures the image noise model, the Rician distribution with parameter σ :

$$p(\hat{\mathbf{y}}_i | \mathbf{y}_i) = \prod_{s \in \text{Pixels}} \frac{\hat{\mathbf{y}}_i[s]}{\sigma^2} \exp\left(-\frac{(\hat{\mathbf{y}}_i[s])^2 + (\mathbf{y}_i[s])^2}{2\sigma^2}\right) \times \text{I}_0\left(\frac{\hat{\mathbf{y}}_i[s] \mathbf{y}_i[s]}{\sigma^2}\right), \quad (3)$$

where I_0 is the zeroth-order-modified Bessel function of the first kind, and σ is the standard deviation of the Gaussian noise in the real and the imaginary images, which is assumed to be equal and spatially invariant. The modified total variation (TV_ϕ) of images is employed as image prior: , i.e. $p(\mathbf{y}_1, \dots, \mathbf{y}_N) \propto \exp(-\lambda \text{TV}_\phi(\mathbf{y}_1, \dots, \mathbf{y}_N))$, with

$$\text{TV}_\phi(\mathbf{y}_1, \dots, \mathbf{y}_N) = \sum_{s \in \text{Pixels}} \phi\left(\sum_{i=1, \dots, N; k=1, 2} (\nabla_k \mathbf{y}_i[s])^2\right), \quad (4)$$

where $\phi(x) = \sqrt{c + x/\tau^2}$, τ scales the gradient magnitude, c controls the smoothness of low contrast regions, $\nabla_k \in \mathbb{R}^{P \times P}$ is the gradient operator in the k -th direction, $[\cdot]$ indexes the vector (s -th element of $\nabla_k \mathbf{y}_i$ in the formula above) and parameter λ controls the amount of regularization.

This denoising formulation is extensively used in image processing, and incorporates the edge information from all components of the image. Rank constraint on matrix $[\mathbf{y}_1, \dots, \mathbf{y}_N]$ introduced by Lam *et al.* in [9] showed significant improvement compared to other methods, such as non-local means denoising [10], and will be considered in this work as the state-of-the-art for denoising *aligned* DW-MRI data and referred to as rank-edge denoising (RE-denoising).

2.2 Registration-Guided (RG) Denoising

Now consider that DW images \mathbf{y}_i are spatially misaligned and all pairwise mapping estimates are given $\{\mathcal{T}_{ij}\}_{i,j=1}^N$, such that $\mathcal{T}_{ij}(\mathbf{y}_i) \approx \mathbf{y}_j$. If all transformations $\{\mathcal{T}_{ij}\}$ were correct, we could use them to warp all images into the common coordinate frame and perform RE-denoising. However, in practice the registrations are not ideal. Moreover, if out-of-plane motion is present, these 2D transformations do not even exist. Ignoring the registration inaccuracies can amplify noise near misaligned edges, decrease denoising quality and create noisy structures. Ideally we want to have a local registration accuracy estimation, that would indicate for every image pixel, if we can use information from the other warped images. Here we propose to enforce *sparse* image edges consistency across the images instead of regularizing them directly. We use a compressed sensing approach to maximize the region of gradient consistency. Here we propose to extend (2), yielding the following registration-guided (RG) denoising model:

$$\min_{\{\mathbf{y}_i\}} - \sum_{i=1}^N \log p(\hat{\mathbf{y}}_i | \mathbf{y}_i) + \lambda \sum_i \text{TV}_\phi(\mathbf{y}_i) + \beta \sum_{i,j} \sum_{k=1,2} \underbrace{\|\nabla_k \mathbf{y}_j - \nabla_k \mathbf{R}_{ij} \mathbf{y}_i\|_1}_{\text{sparse gradients consistency}}, \quad (5)$$

where parameter β weights the consistency of the gradients of images i and j . $\mathbf{R}_{ij} = \mathbf{R}(\mathcal{T}_{ij}) \in \mathbb{R}^{P \times P}$ is a sparse matrix which warps an image with a given transformation and depends on the image interpolation scheme $\mathcal{T}_{ij}(\mathbf{y}_i) = \mathbf{R}_{ij} \mathbf{y}_i$. Since the ℓ_1 -norm is a convex relaxation of the cardinality measure, this sparsity-inducing term encourages the least number of non-aligned edges.

The problem (5) is not smooth and cannot be solved with ordinary gradient descent methods. We apply the theory of duality, and use the ADMM [11] algorithm. Problem (5) can be transformed to the following equivalent form:

$$\begin{aligned} \min_{\mathbf{y}_i, \mathbf{f}_i, \mathbf{z}_{ijk}} & - \sum_i \log p(\hat{\mathbf{y}}_i | \mathbf{f}_i) + \lambda \sum_i \sum_s \phi \left(\sum_{k=1,2} (\mathbf{z}_{iik}[s])^2 \right) + \beta \sum_{i,j} \sum_{k=1}^2 \|\mathbf{t}_{ijk}\|_1, \\ \text{s.t.} & \quad \mathbf{f}_i = \mathbf{y}_i, \quad \mathbf{z}_{ijk} = \nabla_k \mathbf{R}_{ij} \mathbf{y}_i, \quad \mathbf{t}_{ijk} = \nabla_k \mathbf{y}_j - \mathbf{z}_{ijk}, \quad \forall i, j, k \end{aligned} \quad (6)$$

In this form the problem can be solved with an iterative ADMM scheme described in [11].

Algorithm 1. Proposed iterative registration and denoising scheme. The denoising step with the RE-method is performed in the following manner: all images are transformed to the i -th coordinate frame, then the i -th image is denoised with the RE-method and stored as $\mathbf{y}_i^{(k+1)}$. In practice the stopping criteria is reached after 4-10 iterations with $\mathcal{F}_{\text{tol}} = 10^{-2}$.

```

Initialize  $\{\mathbf{y}_i\}^{(1)}$  with single image denoising,  $k := 1$ 
Repeat:
  for  $i := 1$  to  $N$ 
    for  $j := 1$  to  $N$ 
       $\mathcal{T}_{ij}^{(k+1)} \leftarrow \text{register } \mathbf{y}_i^{(k)} \text{ to } \mathbf{y}_j^{(k)} \text{ with (7)}$ 
    rof
  rof
   $\{\mathbf{y}_i\}^{(k+1)} \leftarrow \text{denoise images with RG- or RE- method}$ 
   $k \leftarrow k + 1$ 
   $\mathcal{F}^{(k+1)} = \frac{1}{N^2(\#\text{Pixels})} \sum_{ij} \|\mathbf{y}_j^{(k+1)} - \mathcal{T}_{ij}^{(k+1)}(\mathbf{y}_i^{(k+1)})\|_2$ 
while  $\|\mathcal{F}^{(k+1)} - \mathcal{F}^{(k)}\| \geq \mathcal{F}_{\text{tol}}$  and  $k \leq k_{\text{max}}$ .

```

2.3 Simultaneous Denoising and Registration

Given two images \mathbf{y}_i and \mathbf{y}_j the registration problem can be modelled as the following optimization task:

$$\underset{\mathcal{T}_{ij} \in \text{Affine}}{\text{minimize}} \text{LNCC}(\mathbf{y}_j, \mathcal{T}_{ij}(\mathbf{y}_i)), \quad (7)$$

where LNCC is local normalized cross correlation image metric, a multi-model image similarity metric which is insensitive to local linear contrast changes and can be computed efficiently [12]. Image registration is a highly nonlinear and non-convex problem. To deal with this problems, while aligning low SNR images, we propose to iteratively perform denoising and registration of denoised images. Reducing the image noise should enhance image registration results. The procedure is described in the Algorithm 1.

3 Results

To enable qualitative evaluation, we build on a high-resolution, high-quality, motion-free *ex vivo* canine heart dataset [13] as ground truth and simulate data of *in vivo* quality. The publicly available¹ *ex vivo* data was acquired using a 3D fast spin-echo sequence. Twenty diffusion encoding gradients were used for each imaging slice with in-plane resolutions of $0.31 \times 0.31 \text{mm}^2$ and slice thickness of 0.8 mm. The imaging slices were then stacked and downsampled to $0.6 \times 0.6 \times 1.6 \text{mm}^3$ resolution to produce a plausible *in vivo* gold standard tensor model, to evaluate recovery from simulated noise and spatial transformations as described in the next sections.

¹ <http://cvrgrid.org/data/ex-vivo>

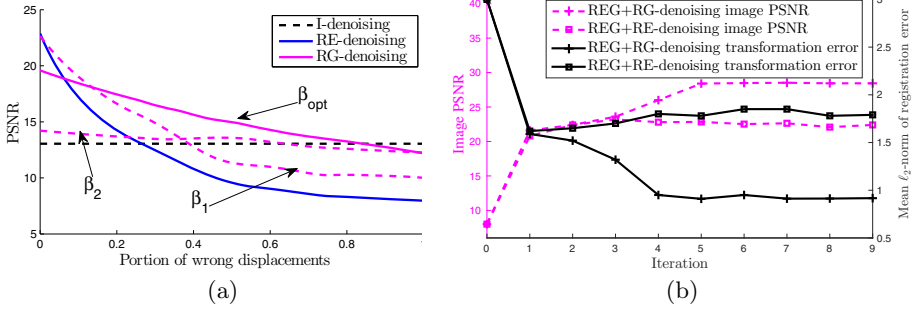


Fig. 1. (a) Dependence between denoising quality (mean image PSNR), registration accuracy and parameter β . The pixel displacement is considered to be wrong, if its length is larger than 1 pixel. $\beta_{opt} = 0.02, \beta_1 = 0.08, \beta_2 = 0.003$ (b) Mean image denoising and registration performance on the synthetic dataset.

Registration-Guided Denoising. First, we test the ability of the proposed RG-denoising to improve image quality despite inaccurate transformations. For this purpose we fixed a reference imaging slice and created four DW images, deformed with random in-plane ground truth affine transformation M_{ij} such that $|\det(M_{ij}) - 1| \leq 0.05$. Random affine transformation matrices with the same properties were then added to produce erroneous transformations \hat{T}_{ij} . Finally, images were degraded with additive Rician noise ($\sigma = 10$). We solve (5) to obtain denoised images and compare the peak SNR (PSNR) of the images.

We compare our RG-denoising with two extreme denoising variants: independent image TV denoising (I-denoising) e.g. solving (2) separately for each image without rank constraint, and RE-denoising. Obviously, if all the transformations are correct, then RE-denoising will give the best possible result for a given edge prior. However, any misalignment will degrade averaging quality. I-denoising does not use any registration information and therefore does not depend on the registration quality. Large (see β in Figure 1a) values of β tend to favor gradients consistency, which results in low restoration quality in cases when there are misaligned images (β_1 Fig. 1a). With small β values, the method ignores gradients consistency and behaves like I-denoising (β_2 Fig. 1a). We could observe that there exist optimal values β_{opt} , such that denoising quality is close to the best when all registrations are correct, and a little worse than single image denoising, when all are wrong (β_{opt} Fig. 1a).

Second, we show that our method is able to improve registration and denoising quality simultaneously. We took the same set of four images and executed Algorithm 1 with RG- and RE- denoising methods. Figure 1(b) shows that our method improves on RE-denoising and registration, which led to more accurate registration estimates as well. Ignoring registration inaccuracies during the denoising step can degrade the estimation results.

DTI Quantitative Assessment. To model the *in vivo* acquisition process accurately, for each axial imaging plane, 10 noncollinear diffusion gradients were

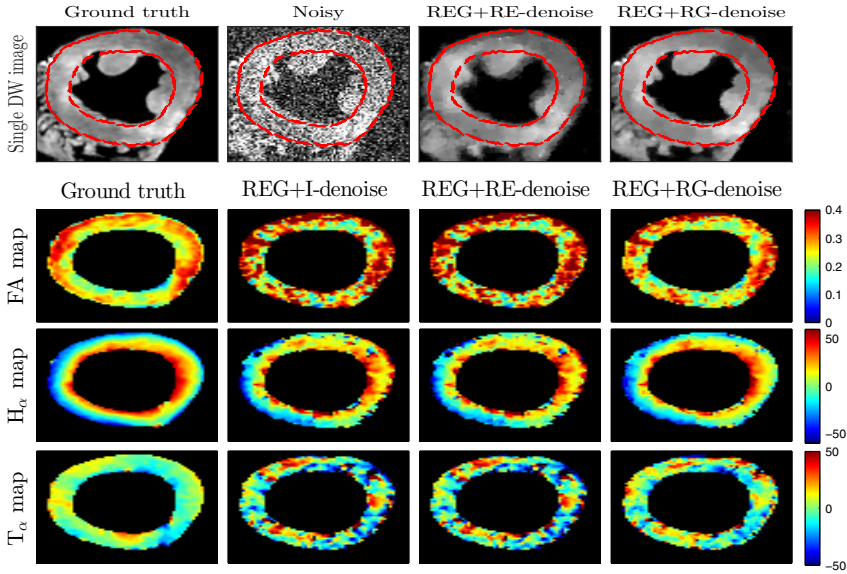


Fig. 2. Comparison of DW intensity, FA, helix and transverse angle maps, from different iterative image registration and denoising schemes. The provided ventricle-myocardium segmentation is shown as red lines. Note the edge fuzziness of the RE-denoising based method, caused by misalignments.

chosen. The proposed method was tested for affine transformations, as these capture the components of cardiac deformation due to respiration, e.g. [14], but can also successfully be applied to non-affine deformations (tests not included). For each gradient direction a random affine mapping M_i was applied to the imaging plane, such that the inclination of the mapped plane to the original is less than 10° and $|\det(M) - 1| \leq 0.05$. Corresponding DW images were then computed according to (1) using the finite strain (FS) reorientation strategy described in [15]. After that, Rician noise with $\sigma = 12$ was added to the image, yielding \hat{y}_i . These 10 DW images were denoised and spatially aligned using three methods: (i) registration and I-denoising, (ii) iterative registration and RE-denoising, (iii) iterative registration and RG-denoising. Six iterations of the Algorithm 1 were executed with the following denoising parameters: $\beta = 0.012$, $\lambda = 0.2$, $\tau = 3$, $c = 1$ and a $7 \times 7\text{px}^2$ region was used for the LNCC. A standard least-squares approach together with the FS reorientation strategy was applied to the denoised images using the estimated transformations to produce DT maps of the reference plane. To compare the results of the reconstruction we analyzed the following characteristics of the DT map: (i) fractional anisotropy (FA) RMSE, (ii) mean affine-invariant Riemannian distance [16] between reconstructed and ground truth tensors: $\Delta_{AI}(D_1, D_2) = \|\log(D_1^{-1/2}D_2D_1^{-1/2})\|_F$ and (iii) myocardial fiber helix angle (H_α) and transverse angle (T_α) [17] distributions.

The first row in Figure 2 shows the gold standard DW image together with the denoising results for a single fixed diffusion gradient direction. As can be seen, the

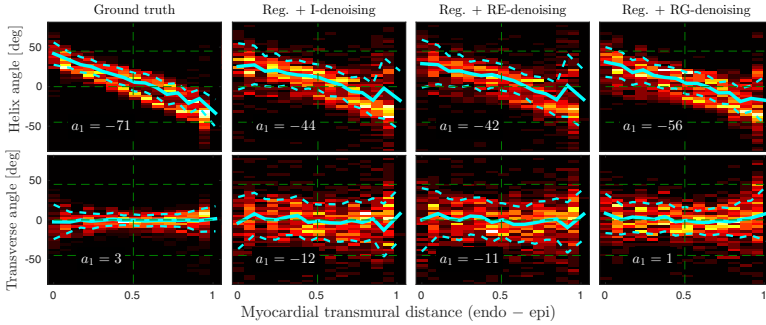


Fig. 3. Myocardial fibers helix and transverse angle distribution with respect to transmural abscissa together with cyan lines showing mean and one standard deviation. a_1 is the regression slope of the linear fit.

Table 1. DTI reconstruction measures computed in the myocardium. Columns $H_{\alpha-\sigma}$ and $T_{\alpha-\sigma}$ state the standard deviation of the linear model fit for H_{α} and T_{α} .

Method	PSNR	FA-RMSE	Δ_{AI}	H_{α} -RMSE	$H_{\alpha-\sigma}$	T_{α} -RMSE	$T_{\alpha-\sigma}$
I-denoising	22.8	0.37	0.17	13.7°	28.4°	19.8°	29.1°
RE-denoising	21.4	0.39	0.18	14.0°	28.1°	19.1°	29.8°
RG-denoising	27.6	0.28	0.13	11.5°	20.4°	14.6°	25.8°
No denoising	16.1	0.49	0.70	29.4°	39.1°	31.2°	43.1°

proposed (REG+RG-denoise) noise reduction is more effective, especially at the myocardium edges. Tensor estimate quality and fibre geometry reconstruction also benefit from the proposed method. Illustration of fiber inclination distribution is shown in Figure 3. Studies indicate [18] that there should be linear dependence between helix angle and transmural myocardium distance. The transverse angle is reported to be close to zero inside the myocardium. Standard deviations of these angles from the linear models are reported in the Table 1 together with other performance metrics. We notice that iterative registration with RE-denoising outperforms independent image denoising, which illustrates the danger of ignoring the misalignment errors. The proposed RG-denoising based method showed substantial improvement in denoising and tensor estimation quality.

4 Conclusions

In this paper we have addressed the problem of alignment and denoising of DWI data. Quantitative evaluation, based on simulations from *ex vivo* data, shows that the standard DWI denoising methods can degrade reconstruction results, when either poor alignment or out-of-plane motion occurs. Our proposed method based on a robust groupwise denoising approach, allows to deal with foregoing issues. The method showed qualitative improvement over standard techniques both in the image denoising quality (+21% PSNR) and anatomical characteristics, such as helix (-18% RMSE) and transversal angles of the myocardial fibers.

References

1. Pierpaoli, C.: Artifacts in diffusion MRI. In: *Diffusion MRI: Theory, Methods and Applications*, pp. 303–318. Oxford University Press, New York (2010)
2. Toussaint, N., Stoeck, C.T., Schaeffter, T., Kozerke, S., Sermesant, M., Batchelor, P.: In vivo human cardiac fibre architecture estimation using shape-based diffusion tensor processing. *Medical Image Analysis* 17(8), 1243–1255 (2013)
3. Han, J., Berkels, B., Rumpf, M., Hornegger, J., Droske, M., Fried, M., Scorzin, J., Schaller, C.: A variational framework for joint image registration, denoising and edge detection. In: *Bildv. Für Die Med.* 2006, pp. 246–250. Springer, Heidelberg (2006)
4. Telea, A.C., Preusser, T., Garbe, C.S., Droske, M., Rumpf, M.: A variational approach to joint denoising, edge detection and motion estimation. In: Franke, K., Müller, K.-R., Nickolay, B., Schäfer, R. (eds.) *DAGM 2006. LNCS*, vol. 4174, pp. 525–535. Springer, Heidelberg (2006)
5. Sanches, J.M., Marques, J.S.: Joint image registration and volume reconstruction for 3D ultrasound. *Pattern Recognition Letters* 24(4), 791–800 (2003)
6. Lombaert, H., Cheriet, F.: Simultaneous image denoising and registration using graph cuts: Application to corrupted medical images. In: *ISSPA*, pp. 264–268. IEEE (2012)
7. Lempitsky, V., Rother, C., Blake, A.: Logcut-efficient graph cut optimization for markov random fields. In: *ICCV*, pp. 1–8. IEEE (2007)
8. Getreuer, P.: Rudin-Osher-Fatemi total variation denoising using split Bregman. *IPOL* 10 (2012)
9. Lam, F., Babacan, D., Haldar, J., Weiner, M., Schuff, N., Liang, Z.: Denoising diffusion-weighted magnitude MR images using rank and edge constraints. *Magnetic Resonance in Medicine* 71(3), 1272–1284 (2014)
10. Wiest-Daesslé, N., Prima, S., Coupé, P., Morrissey, S.P., Barillot, C.: Non-local means variants for denoising of diffusion-weighted and diffusion tensor MRI. In: Ayache, N., Ourselin, S., Maeder, A. (eds.) *MICCAI 2007, Part II. LNCS*, vol. 4792, pp. 344–351. Springer, Heidelberg (2007)
11. Boyd, S., Parikh, N., Chu, E., Peleato, B., Eckstein, J.: Distributed optimization and statistical learning via the alternating direction method of multipliers. *Foundations and Trends in ML* 3(1), 1–122 (2011)
12. Cachier, P., Bardinet, E., Dormont, D., Pennec, X., Ayache, N.: Iconic feature based nonrigid registration: the PASHA algorithm. *Computer Vision and Image Understanding* 89(2), 272–298 (2003)
13. Helm, P., Younes, L., Beg, M., Ennis, D., Leclercq, C., Faris, O., McVeigh, E., Kass, D., Miller, M., Winslow, R.: Evidence of structural remodeling in the dyssynchronous failing heart. *Circulation Research* 98(1), 125–132 (2006)
14. King, A., Rhode, K., Razavi, R., Schaeffter, T.: An adaptive and predictive respiratory motion model for image-guided interventions: theory and first clinical application. *T. Med. Imag.* 28(12), 2020–2032 (2009)
15. Alexander, D., Pierpaoli, C., Basser, P., Gee, J.: Spatial transformations of diffusion tensor magnetic resonance images. *T. Med. Imag.* 20(11), 1131–1139 (2001)
16. Fillard, P., Pennec, X., Arsigny, V., Ayache, N.: Clinical DT-MRI estimation, smoothing, and fiber tracking with log-Euclidean metrics. *T. Med. Imag.* 26(11), 1472–1482 (2007)
17. Scollan, D., Holmes, A., Winslow, R., Forder, J.: Histological validation of myocardial microstructure obtained from diffusion tensor magnetic resonance imaging. *Am. J. of Physiology-Heart and Circulatory Phys.* 275(6), H2308–H2318 (1998)
18. Lombaert, H., Peyrat, J., Croisille, P., Rapacchi, S., Fanton, L., Clarysse, P., Magnin, I., Delingette, H., Ayache, N.: Human atlas of the cardiac fiber architecture: study on a healthy population. *T. Med. Imag.* 31(7), 1436–1447 (2012)